Core and margin in warm convective clouds. Part I: core types and evolution during a cloud's lifetime

[1]Reuven H. Heiblum, [1]Lital Pinto, [1]Orit Altaratz, [1,2]Guy Dagan, [1]Ilan Koren

[1]Department of Earth and Planetary Sciences, Weizmann Institute of Science, Rehovot, Israel

[2]now at: Atmospheric, Oceanic and Planetary Physics, Department of Physics, University of Oxford, UK

Corresponding Email – ilan.koren@weizmann.ac.il

Abstract:

The properties of a warm convective cloud are determined by the competition between the growth and dissipation processes occurring within it. One way to observe and follow this competition is by partitioning the cloud to core and margin regions. Here we look at three core definitions: positive vertical velocity (W_{core}), supersaturation (RH_{core}), and positive buoyancy (B_{core}), and follow their evolution throughout the lifetime of warm convective clouds.

Using single cloud and cloud field simulations with bin-microphysics schemes, we show that the different core types tend to be subsets of one another in the following order: $B_{core} \subseteq RH_{core} \subseteq W_{core}$. This property is seen for several different thermodynamic profile initializations, and is generally maintained during the growing and mature stages of a cloud's lifetime. This finding is in line with previous works and theoretical predictions showing that cumulus clouds may be dominated by negative buoyancy at certain stages of their lifetime.

During its mature and growth stage, the cloud and its cores are centered at a similar location. During cloud dissipation the cores show less overlap, typically reduce in size, and migrate from the cloud centroid. In some cases, buoyancy cores can reemerge and often reside at the cloud periphery. Thus, the core-shell model of a positively buoyant center surrounded by negatively buoyant shell only applies to a fraction of the cloud lifetime.

1. Introduction

Clouds are important players in the climate system (Trenberth et al., 2009), and currently constitute one of the largest uncertainties in climate and climate change research (IPCC, 2013). One of the reasons for this large uncertainty is the complexity created by opposing processes that occur at the same time but in different locations within a cloud. Although a cloud is generally considered as a single entity, physically, it can be partitioned to two main regions: i) a core region, where mainly cloud growth processes occur (i.e. condensation – accumulation of cloud mass), and ii) a margin region, where cloud suppression processes occur (i.e. evaporation - loss of cloud mass). Changes in thermodynamic or microphysical (aerosol) conditions impact the processes in both regions (sometimes in different ways), and thus the resultant total cloud properties (Dagan et al., 2015). To better understand cloud properties and their evolution in time, it is necessary to understand the interplay between physical processes within the core and margin regions (and the way they are affected by perturbations in the environmental conditions).

Considering convective clouds, there are several objective measures that have been used in previous works for separating a cloud's core from its margins (will be referred to as physical cores hereafter). In deep convective cloud simulations the core is usually defined by the updrafts' magnitude using a certain threshold, usually $W>1$ $m \cdot s^{-1}$ (Khairoutdinov et al., 2009; Kumar et al., 2015; Lebo and Seinfeld, 2011; Morrison, 2012). Studies on warm cumulus clouds have defined the clouds' core as parts with positive buoyancy and positive updrafts (de Roode et al., 2012; Dawe and Austin, 2012; Heus and Jonker, 2008; Siebesma and Cuijpers, 1995) or solely regions with positively buoyancy (Heus and Seifert, 2013; Seigel, 2014). More recently, cloud partition to regions of supersaturation and sub-saturation has been used to define the cloud core in single cloud simulations (Dagan et al., 2015).

For simplicity, we focus on warm convective clouds (only contain liquid water), avoiding the additional complexity and uncertainties associated with mixed phase and ice phase microphysics. The common assumption when partitioning a convective cloud to its physical core and margin is that that the cloud core is at its geometrical center and the peripheral regions (i.e. edges) are the margin. Previous observational (Heus et al., 2009a; Rodts et al., 2003; Wang et al., 2009) and numerical (Heus and Jonker, 2008;

Jonker et al., 2008; Seigel, 2014) works have studied the gradients of cloud thermodynamic properties from cloud center to edge, and suggest that a cloud is best described by a core-shell model. This model assumes a core with positive vertical velocity and buoyancy, surrounded by a shell with negative vertical velocity and buoyancy. The shell is the region where mixing between cloudy and environmental air parcels occurs, leading to evaporative cooling → decrease in buoyancy → decrease in vertical velocity.

Based on previous findings, here we explore the partition of clouds to core and margin using three different objective core definitions where the cloud core threshold is set to be a positive value (of buoyancy, vertical velocity, or supersaturation). Cloud buoyancy (B) can be approximated by the following formula:

$$B = g \cdot \left(\frac{\theta'}{\theta_o} + 0.61 q_v' - q_l\right) \quad (1),$$

Where θ_o represents the reference state potential temperature, q_v is the water vapor mixing ratio, and q_l is the liquid water content. The (') stands for the deviation from the reference state per height (Wang et al., 2009). Buoyancy is a measure for the vertical acceleration and its integral is the convective potential energy. Latent heat release during moist adiabatic ascent fuels positive buoyancy and clouds' growth, while evaporation and subsequent cooling drives cloud decay (de Roode, 2008; Betts, 1973). The prevalence of negatively buoyancy parcels at the cloud edges due to mixing and evaporation is a well-known phenomenon (Morrison, 2017). Mixing diagrams have been used to assess this effect (de Roode, 2008; Paluch, 1979; Taylor and Baker, 1991), and are at the root of convective parameterization schemes (Emanuel, 1991; Gregory and Rowntree, 1990; Kain and Fritsch, 1990) and parameterizations of entrainment and detrainment in cumulus clouds (de Rooy and Siebesma, 2008; Derbyshire et al., 2011).

Neglecting cases of air flow near obstacles or air mass fronts, buoyancy is the main source for vertical momentum in the cloud. In its simplest form, the vertical velocity (w) in the cloud can be approximated by the convective available potential energy (CAPE) of the vertical column up to that height (Rennó and Ingersoll, 1996; Williams and Stanfill, 2002; Yano et al., 2005):

$$0.5w^2(h) = \int_{h_0}^{h} B(z)\, dz = CAPE(h) \quad (2).$$

Here we define CAPE to be the vertical integral of buoyancy from the lowest level of positive buoyancy (h_0, initiation of vertical velocity) to an arbitrary top height (h). Usually, the CAPE serves as a theoretical upper limit, and the vertical velocity is smaller due to multiple effects (de Roode et al., 2012), most importantly the perturbation pressure gradient force (which oppose the air motion) and mixing with the environment (entrainment/detrainment) (de Roode et al., 2012; Morrison, 2016a; Peters, 2016). Recent studies have shown that entrainment effects on vertical velocity are of second order, and a rising thermal shows a balance between buoyancy and the perturbation pressure gradient (Hernandez-Deckers and Sherwood, 2016; Romps and Charn, 2015), the latter acting as a drag force on the updrafts. Nevertheless, initial updraft and environmental conditions play a crucial role in determining the magnitude of mixing effects on buoyancy, and thus also the vertical velocity profile in the cloud (Morrison, 2016a, 2016b, 2017).

The supersaturation (S, where S=1 is 100% relative humidity) core definition (S-1>0 or RH>100%) partitions the cloud core and margin to areas of condensation and evaporation. Since we consider hconvective clouds, the only driver of supersaturation during cloud growth is upward vertical motion of air. Neglecting mixing with the environment, S and w can be linked as follows:

$$\frac{dS}{dt} = Q_1 w - Q_2 \frac{dq_l}{dt} \quad (3),$$

where Q_1,Q_2 are thermodynamic factors (Rogers and Yau, 1989). The thermodynamic factors are nearly insensitive to pressure for temperature above 0^{o}C, and both weakly decrease (less than 15% net change) with temperature increase between 0^{o}C and 30^{o}C (Pinsky et al., 2013). The first term on the right-hand side is related to the change in the supersaturation due to adiabatic cooling or heating of the moist air (due to vertical motion). The second term is related to the change in the supersaturation due to condensation/evaporation of water vapor/drops. Hence, the supersaturation in a rising parcel depends on the magnitude of the updraft and on the condensation rate of vapor to drops (a sink term). The latter is proportional to the concentration of aerosols in the cloud (Reutter et al., 2009; Seiki and Nakajima, 2014), which serve as cloud condensation nuclei (CCN) for cloud droplets. In Part II of this work we demonstrate some of the insights gained by investigating differences between the different cores properties and their time evolution when changing the aerosol loading.

The purpose of this part of the work (part I) is to compare and understand the differences between the three basic definitions of cloud core (i.e. $W_{core}, RH_{core}, B_{core}$) throughout a convective cloud's lifetime, using both theoretical arguments and numerical simulations. It should be noted that the bin-microphysical schemes used here calculate saturation explicitly, by solving the diffusion growth equation, enabling super- and sub-saturation values in cloudy pixels. This is in contrary to many other works that used bulk-microphysical schemes which rely on saturation adjustment to 100% within the cloud (Khain et al., 2015). This difference may produce significant differences on the evolution of clouds and their cores. Specifically, we aim to answer questions such as:

- Which core type is largest? Which is smallest?
- How do the cores change during the lifetime of a cloud?
- Can different core types be used interchangeably without much effect on analysis results?
- Are the cores centered at the cloud' geometrical center, as expected from the core-shell model?

The differences between the cores' evolution in time shed new light on the competition of processes within a cloud in time and space. Moreover, such an understanding can serve as a guideline to all studies that perform the partition to cloud core and margin, and assist in determining the relevance of a given partition.

2. Methods

2.1. Single cloud model

For single cloud simulations we use the Tel-Aviv University axisymmetric, non-hydrostatic, warm convective single cloud model (TAU-CM). It includes a detailed (explicit) treatment of warm cloud microphysical processes solved by the multi-moment bin method (Feingold et al., 1988, 1991; Tzivion et al., 1989, 1994). The warm microphysical processes included in the model are nucleation, diffusion (i.e. condensation and evaporation), collisional coalescence, breakup and sedimentation (for a more detailed description, see (Reisin et al., 1996)).

Convection was initiated using a thermal perturbation near the surface. A time step of 1 sec is chosen for dynamical computations, and 0.5 sec for the microphysical computations (e.g. condensation-evaporation). The total simulation time is 80 min. There are no radiation processes in the model. The domain size is 5x6 km, with an isotropic 50 m resolution. The model is initialized using a Hawaiian thermodynamic profile, based on the 91285 PHTO Hilo radiosonde at 00Z, 21 Aug, 2007. A typical oceanic size distribution of aerosols is chosen (Altaratz et al., 2008; Jaenicke, 1988), with a total concentration of 500 cm^{-3}. This concentration produced clouds that are non- to weakly- precipitating. In Part II additional aerosol concentrations are considered, including ones which produce heavy precipitation.

2.2. Cloud field model

Warm cumulus cloud fields are simulated using the System for Atmospheric Modeling (SAM) Model (version 6.10.3, for details see webpage: http://rossby.msrc.sunysb.edu/~marat/SAM.html) (Khairoutdinov and Randall, 2003)). SAM is a non-hydrostatic, anelastic model. Cyclic horizontal boundary conditions are used together with damping of gravity waves and maintaining temperature and moisture gradients at the model top. An explicit Spectral Bin Microphysics (SBM) scheme (Khain et al., 2004) is used. The scheme solves the same warm microphysical processes as in the TAU-CM single cloud model, and uses an identical aerosol size distribution and concentration (i.e. 500 cm^{-3}) for the droplet activation process.

We use the BOMEX case study as our benchmark for shallow warm cumulus fields. This case simulates a trade-wind cumulus (TCu) cloud field based on observations made near Barbados during June 1969 (Holland and Rasmusson, 1973). This case study has a well-established initialization setup (sounding, surface fluxes, and surface roughness) and large scale forcing setup (Siebesma et al., 2003). It has been thoroughly tested in many previous studies (Grabowski and Jarecka, 2015; Heus et al., 2009b; Jiang and Feingold, 2006; Xue and Feingold, 2006). To check the robustness of the cloud field results, two additional case studies are simulated: (1) The same Hawaiian profile used to initiate the single cloud model, and (2) a continental shallow cumulus convection cases study (named CASS), based on long term observations taken at the ARM Southern Great Plains (SGP) site (Zhang et al., 2017).

The soundings, large scale forcing, and surface properties used to initialize the model are detailed in previous works (Heiblum et al., 2016a; Siebesma et al., 2003; Zhang et al., 2017). The domain size is 12.8 km x 12.8 km x 4 km for BOMEX, 12.8 km x 12.8 km x 5 km for Hawaii, and 25.6 km x 25.6 km x 16 km for CASS. The grid size is set to 100 m in the horizontal direction and 40 m in the vertical direction for all simulations. For CASS, above a height of 5 km the vertical grid size gradually increases to 1km. The time step for computation is 1 s for all simulations, with a total runtime of 8 hours for BOMEX and Hawaii, and 12 hours for CASS. The initial temperature perturbations (randomly chosen within ± 0.1ºC) are applied near the surface, during the first time step.

2.3. Physical and Geometrical Core definitions

A cloudy pixel is defined here as a grid-box with liquid water amount that exceeds 0.01 g kg^{-1}. The physical core of the cloud is defined using three different definitions: 1) RH_{core}: all grid boxes for which the relative humidity (RH) exceeds 100%, 2) B_{core}: buoyancy (see definition in Eq. (1)) above zero. The buoyancy is determined in each time step by comparing each cloudy pixel with the mean thermodynamic conditions for all non-cloudy pixels per vertical height, and 3) W_{core}: vertical velocity above zero. These definitions apply for both the single cloud and cloud field model simulations used here. We note that setting the core thresholds to positive values (>0) may increase the amount of non-convective pixels which are classified as part of a physical core, especially for the W_{core}. Indeed, taking higher thresholds for the updrafts decreases the W_{core} extent and reduces the variance. Nevertheless, any threshold taken is subjective in nature, while the positive vertical velocity definition is process based and objective.

The centroid (i.e. mean location in each of the axes) is used here to represent the geometrical location of the total cloud (i.e. cloud geometrical core) and its specific physical cores. The distances between the total cloud and its cores' centroids (D_{norm}), as presented here, are normalized to cloud size to reflect the relative distance between the two centroids, where $D_{norm} = 0$ indicates coincident physical and geometrical cores and $D_{norm} = 1$ indicates a physical core located at the cloud boundary. The single cloud simulations rely on an axisymmetric model and thus all centroids are

horizontally located on the center axis while vertical deviations are permitted. For this model the distance is normalized by half the cloud's thickness. For the cloud field simulations both horizontal and vertical deviations are possible, therefore distances are normalized by the cloud's volume radius.

2.4. Center of gravity vs. Mass (CvM) phase space

Recent studies (Heiblum et al., 2016a, 2016b) suggested the Center-of-Gravity vs. Mass (CvM) phase space as a useful approach to reduce the high dimensionally and to study results of large statistics of clouds during different stages of their lifetimes (such as seen in cloud fields). In this space, the Center-of-Gravity (COG) height and mass of each cloud in the field at each output time step (taken here to be 1 min) are collected and projected in the CvM phase space. This enables a compact view of all clouds in the simulation during all stages of their lifetimes, with the main disadvantage being the loss of grid-size resolution information on in-cloud dynamical processes. Although the scatter of clouds in the CvM is sensitive to the microphysical and thermodynamic settings of the cloud field, it was shown that the different subspaces in the CvM space correspond to different cloud processes and stages (Heiblum et al., 2016a, 2016b). The lifetime of a cloud can be described by a trajectory on this phase space.

A schematic illustration of the CvM space in shown in Fig. 1. Most clouds are confined between the adiabat (curved dashed line) and the inversion layer base (horizontal dashed line). The adiabat curve corresponds to the theoretical evolution of a moist adiabat 1D cloud column in the CvM space. The large majority of clouds form within the growing branch (yellow shade) at the bottom left part of the space, adjacent to the adiabat. Clouds then follow the growing trajectory (grow in both COG and mass) to some maximal values. The growing branch deviates from the adiabat at large masses depending on the degree of sub-adiabaticity of the cloud field. After or during the growth stage of clouds, they may undergo the following processes: i) dissipate via a reverse trajectory along the growing one, ii) dissipate via a gradual dissipation trajectory (magenta shade), iii) shed off small mass cloud fragments (red shades), iv) in the case of precipitating clouds, they can shed off cloud fragments in the sub-cloudy layer (grey shade). The former two processes form continuous trajectories in the CvM space, while the latter two processes create disconnected subspaces.

2.5. Cloud tracking

To follow the evolution of individual clouds within a cloud field we use an automated 3D cloud tracking algorithm (see (Heiblum et al., 2016a) for details). It enables tracking of Continuous Cloud Entities (CCEs) from formation to dissipation, even if interactions between clouds (splitting or merging) occur during that lifetime. A CCE initiates as a new cloud forming in the field, and is tracked on the condition that it retains the majority (>50%) of its mass during an interaction event if occurs. Thus, a CCE can terminate due to either cloud dissipation or cloud interactions.

3. Theoretical estimations for different core sizes

Here we propose simple physical considerations to evaluate the differences in cloud partition to core and margin using different definitions. The arguments rely on key findings from previous works (see Sect. 1) with aim to gain intuitive understanding of the potential differences between the core types. It is convenient to separate the analysis to an adiabatic case, and then add another layer of complexity and consider the effects of mixing of cloudy and non-cloudy air. In this theoretical derivation saturation adjustment to RH=100% is assumed for both cases, while in the other models used in this study, transient super- and sub-saturated cloudy parcels are treated (more realistic).

3.1. Adiabatic case – no mixing

Considering moist-adiabatic ascent, the excess vapor above saturation is instantaneously converted to liquid (saturation adjustment). Thus, the adiabatic cloud is saturated (S=1) throughout its vertical profile, and only W_{core} and B_{core} differences can be considered. It is assumed that the adiabatic convective cloud is initiated by positive buoyancy initiating from the sub-cloudy layer. As long as the cloud is growing it should have positive CAPE and will experience positive w throughout the column even if the local buoyancy at specific height is negative. Eventually the cloud must decelerate due to negative buoyancy and reach a top height, where CAPE = 0 and $w = 0$. Hence, for the adiabatic column case, B_{core} is always a proper subset of W_{core} ($B_{core} \subset W_{core}$). These effects are commonly seen in warm convective cloud fields

where permanent vertical layers of negative buoyancy (but with updrafts) within clouds typically exist at the bottom and top regions of the cloudy layer (de Roode and Bretherton, 2003; Betts, 1973; Garstang and Betts, 1974; Grant and Lock, 2004; Heus et al., 2009b; Neggers et al., 2007).

3.2. Cloud parcel entrainment model

A mixing model between a saturated (cloudy) parcel and a dry (environment) parcel is used to illustrate the effects of mixing on the different core types. The details of these theoretical calculations are shown in Appendix A. The initial cloudy parcel is assumed to be saturated (part of RH_{core}), have positive vertical velocity (part of W_{core}), and experience either positive or negative buoyancy (part of B_{core} or B_{margin}), as is seen for the adiabatic column case. Additionally, mixing is assumed to be isobaric, and in a steady environment where the average temperature of the environment per a given height does not change. The resultant mixed parcel will have lower humidity content and lower LWC as compared to the initial cloudy parcel, and a new temperature. In nearly all cases (beside in an extremely humid environment) the mixed parcel will be sub-saturated and evaporation of LWC will occur. Evaporation ceases when equilibrium is reached due to air saturation (S=1) or due to complete evaporation of the droplets (which means S<1, and the mixed parcel is no longer cloudy since it has no liquid water content).

In addition to mixing between cloudy (core or margin) and non-cloudy parcels, mixing between core and margin parcels (within the cloud) also occurs. This mixing process can be considered as "entrainment-like" with respect to the cloud core. Considering the changes in the W_{core} and RH_{core}, there is no fundamental difference in the treatment of mixing of cloudy and non-cloudy parcels, or mixing between core and margin (because the margins and the environment are typically sub-saturated and experience negative vertical velocity). However, for the changes in the B_{core} after mixing, there exists a fundamental difference between mixing *with* the reference temperature/humidity state (in the case of mixing with the environment) and mixing *given* a reference temperature/humidity state (in mixing between B_{core} and B_{margin}). Thus, it is interesting to check the effects of mixing between B_{core} and B_{margin} parcels on the

total extent of the B_{core} with respect to the other two core types. The details of this second case are shown in Appendix B.

3.2.1. Effects of non-cloudy entrainment on buoyancy

When mixed with non-cloudy air, the change in buoyancy of the initial cloudy parcel (which is a part of W_{core} and RH_{core} and either B_{core} or B_{margin}) happens due to both mixing and evaporation processes. The theoretical calculations show that for all relevant temperatures (~0^{o}C to 30^{o}C, representing warm Cu), the change in the parcel's buoyancy due to evaporation alone will always be negative (see appendix A). It is because the negative effect of the temperature decrease outweighs the positive effects of the humidity increase and water loading decrease. Nevertheless, the total change in the buoyancy (due to both mixing and evaporation) depends on the initial temperature, relative humidity, and liquid water content of the cloudy and non-cloudy parcels.

In Fig. A1 a wide range of non-cloudy environmental parcels, each with their own thermodynamic conditions, are mixed with a saturated cloud parcel with either positive or negative buoyancy. The main conclusions regarding the effects of such mixing on the buoyancy are as follows:

i. To a first order, the initial buoyancy values are temperature dependent, where a cloudy parcel that is warmer (colder) by more than ~ 0.2^{o}C than the environment will be positively (negatively) buoyant for common values of cloudy layer environment relative humidity (RH>80%).

ii. Parcels that are initially part of B_{core} may only lower their buoyancy due to entrainment, either to positive or negative values depending on the environmental conditions.

iii. The lower the environmental RH, the larger the probability for parcel transition from B_{core} to B_{margin} after entrainment.

iv. Parcels that are initially part of B_{margin} can either increase or decrease their buoyancy value, but never become positively buoyant. The former

case (buoyancy decrease) is expected be more prevalent since it occurs for the smaller range of temperature differences with the environment.

In summary, entrainment is expected to always have a net negative effect on B_{core} extent and B_{margin} values, while evaporation feedbacks serve to maintain RH_{core} in the cloud. Thus, we can predict that B_{core} should be a subset of RH_{core} (i.e. $B_{core} \subseteq RH_{core}$).

3.2.2. Effects of core and margin mixing on buoyancy

We consider the case of mixing between the B_{core} and $B_{margin,}$ meaning positively buoyant and negatively buoyant cloud parcels. For simplicity, we assume both parcels are saturated (S=1, both included in the RH_{core}). As seen above, such conditions exist in both the adiabatic case and in the case where an adiabatic cloud has undergone some entrainment with the environment. The buoyancy differences between the saturated parcels are mainly due to temperature differences, but also due to the increasing saturation vapor pressure with increasing temperature (see Appendix B for details).

In Fig. B1 is it shown that the resultant mixed parcel's buoyancy can be either positive or negative, depending on the magnitude of temperature difference of each parcel (core or margin) from that of the environment. However, in all cases the mixed parcel is supersaturated. This result can be generalized: given two parcels with equal RH but different temperature, the RH of the mixed parcel is always equal or higher than the initial value. Hence, B_{core} can either increase or decrease in extent, while the RH_{core} can only increase due to mixing between saturated B_{core} and B_{margin} parcels. This again strengthens the assumption that B_{core} should be a subset of RH_{core}.

We note that an alternative option for mixing between the core and margin parcels that exist here, where either or both of the parcels are subsaturated so that the mixed parcel is subsaturated as well. In this case evaporation will also occur. As seen in Appendix A, this should further reduce the buoyancy value of the mixed parcel (while increasing the RH).

3.2.3. Effects of entrainment on vertical velocity

The vertical velocity equation dictates that buoyancy is the main production term (de Roode et al., 2012; Romps and Charn, 2015), and is balanced by perturbation pressure gradients and mixing (on grid and sub-grid scales). Thus, all changes of magnitude (and sign) in vertical velocity should lag the changes in buoyancy. This is the basis of convective overshooting and cumulus formation in the transition layer (see Sect. 3.1). It is interesting to assess the magnitude of this effect by quantifying the expected time lag between buoyancy and vertical velocity changes. The calculations in Appendix A indicates negative buoyancy values reaching -0.1 m/s^2 due to entrainment. However, measurements from within clouds show that the temperature deficiency of cloudy parcels with respect to the environment is generally restricted to less than 1^{o}C for cumulus clouds (Burnet and Brenguier, 2010; Malkus, 1957; Sinkevich and Lawson, 2005; Wei et al., 1998), and thus the negative buoyancy should be no more larger than -0.05 m/s^2. This value is closer to current and previous simulations and also observations that show negative buoyancy values within clouds to be confined between -0.001 and -0.01 m/s^2 (de Roode et al., 2012; Ackerman, 1956).

Given an initial vertical velocity of ~ 0.5 m/s, the deceleration due to buoyancy (and reversal to negative vertical velocity) should occur within a typical time range of 1 - 10 minutes. These timescales are much longer than the typical timescales of entrainment (mixing and evaporation that eliminate the B_{core}) which range between 1 – 10 s (Lehmann et al., 2009). Moreover, the fact that a drag force typically balances the buoyancy acceleration (Romps and Charn, 2015) can also contribute to a time lag between effects on buoyancy and subsequent effects on vertical velocity. Therefore, the switching of sign for vertical velocity should occur with substantial delay compared to the reduction of buoyancy, and B_{core} should be a subset of W_{core} (i.e. $B_{core} \subseteq W_{core}$) during the growing and mature stages of a cloud's lifetime.

3.3. The relation between supersaturation and vertical velocity cores

Here we revisit the terms in Eq. 3. A rising parcel initially has no liquid water content, with its only source of supersaturation being the updraft w, and thus initially the RH_{core} should always be a subset of W_{core}. In general, since the sink term $\frac{dLWC}{dt}$ becomes a

source only when S<1 (the condition for evaporation), the only way for a convective cloud to produce supersaturation (i.e. S>1) is by updrafts during all stages of its lifetime. Once supersaturation is achieved, the sink term becomes positive $\frac{dLWC}{dt} > 0$ and balances the updraft source term, so that supersaturation either increases or decreases. At any stage, if downdrafts replace the updrafts within a supersaturated parcel, the consequent change in supersaturation becomes strictly negative (i.e. $\frac{dS}{dt} < 0$). This negative feedback limits the possibility to find supersaturated cloudy parcels with downdrafts. Hence, we can expect the RH_{core} to be smaller than W_{core} during the majority of a cloud's lifetime.

4. Results - Single cloud simulation

The differences between the three types of core definitions are examined during the lifetime of a single cloud (Fig. 2), based on the Hawaiian profile. The cloud's total lifetime is 36 minutes (between t=7 and t=43 min of simulation). Each panel in Fig. 2 presents vertical cross-sections of the three cores (magenta - W_{core}, green - RH_{core}, and yellow - B_{core}) at four points in time (with 10-minute intervals). The cloud has an initial cloud base at 850m, and grows to a maximal top height of 2050 m. The condensation rates (red shades) increase toward the cloud center and the evaporation rates (blue shades) increase toward the cloud edges. Evaporation at the cloud top results in a large eddy below it that contributes to mixing and evaporation at the lateral boundaries of the cloud. Thus, a positive feedback is initiated which leads to cooling, negative buoyancy, and downdrafts. The dissipation of the cloud is accompanied with a rising cloud base and lowering of the cloud top.

During the growing stage (t=10, 20 min), when substantial condensation still occurs within the cloud, all of the cores seem to be self-contained within one another, with B_{core} being the smallest and W_{core} being the largest. During the final dissipation stages, when the cloud shows only evaporation (t=40), W_{core} and RH_{core} disappear while there is still a small B_{core} near the cloud top. Further analysis (see Part II) shows that the entire dissipating cloud is colder and more humid than the environment but downdrafts from the cloud top (see arrows in Fig. 2) promote adiabatic heating, and by that increase the buoyancy in dissipating cloudy pixels, sometimes reaching positive values. These

buoyant pockets will be discussed further in Part II. The results indicate that the three types of physical cores of the cloud are not located around the cloud's geometrical core along the whole cloud lifetime. During cloud growth (i.e. (increase in mass and size) the three types of cores surround the cloud's center, while during late dissipation the B_{core} is at offset from the cloud center.

For a more complete view of the evolution of the three core types in the single cloud case, time series of core fractions are shown in Fig. 3. Panels a and b show the core mass (core mass / total mass - f_{mass}) and volume (core volume / total volume - f_{vol}) fractions out of the cloud's totals. The results are similar for both measures except for the fact that core mass fractions are larger than core volume fractions. This is due to significantly higher LWC per pixel in the cores compared to the margins, which skews the core mass fraction to higher values. Core mass fractions during the main cloud growing stage (between t=7 and t=27 min simulation time) are around 0.7 - 0.85 and core volume fractions are around 0.5 - 0.7. The time series show that as opposed to the W_{core} and RH_{core} fractions which decrease monotonically with time, B_{core} shows a slight increase during stages of cloud growth. In addition, for most of the cloud's lifetime the B_{core} fractions are the smallest and the W_{core} fractions are the largest, except for the final stage of the clouds dissipation where downdrafts from the cloud top creates pockets of positive buoyancy. These pockets are located at the cloud's peripheral regions rather than near the cloud's geometrical center as is typically expected for the cloud's core. In the cloud's center (the geometrical core) the B_{core} is the first one to terminate (at t=32 min) compared to both $W_{core}$and RH_{core} that decay together (at 36 min).

For describing the locations of the physical cores, we examine the normalized distances (D_{norm}) between the cloud's centroid and the cores' centroids. The evolution of these distances is shown in Fig. 3c. At cloud initiation (t=7 min), when the cloud is very small, all cores' centroids coincide with the total cloud centroid location. The B_{core} (and RH_{core} to a much lesser degree) centroid then deviates from the cloud centroid to a normalized distance of 0.27 (t=8 min). As cloud growth proceeds, B_{core} grows and its centroid coincides with the cloud's centroid. All cores' centroids are located near the cloud centroid during the majority of the growing and mature stages of the cloud, showing normalized distances <0.1. During dissipation (t>27 min), the cores' centroid

locations start to distance away from the cloud's geometrical core followed by a reduction in distances due to the rapid loss of cloud volume. As mentioned above, it is shown that the regeneration of positive buoyancy at the end of cloud dissipation (t=40 min) takes place at the cloud edges, with normalized distance >0.5.

Finally, in Fig. 3d the fraction of pixels of each core contained within another core is shown. It can be seen that for the majority of cloud lifetime (up to t=33 min) B_{core} is subset (pixel fraction of 1) of RH_{core}, and the latter is a subset of W_{core}. As expected, the other three permutations of pixel fractions (e.g. W_{core} in B_{core}) show much lower values. The cloudy regions that are not included within B_{core} but are included within the two other cores are exclusively at the cloud's boundaries (see Fig. 2). The same pattern is seen for cloudy regions that are included within W_{core} but not in RH_{core}. During the dissipation stage of the cloud its core subset property (i.e. $B_{core} \subseteq RH_{core} \subseteq W_{core}$) breaks down. Similar temporal evolutions as shown here are seen for the other simulated clouds (with various aerosol concentrations) in part II of this work.

5. Results - Cloud field simulations

5.1. Partition to different core types

To test the robustness of the observed behaviors seen for a single cloud, it is necessary to check whether they also apply to large statistics of clouds in a cloud field. The BOMEX simulation is taken for the analyses here. We discard the first 3 hours of cloud field data, during which the field spins-up and its mean properties are unstable. In Fig. 4 the volume (f_{vol}) and mass (f_{mass}) fractions of the three core types are compared for all clouds (at all output times – every 1 min) in the CvM space. As seen in Fig. 1, the location of specific clouds in the CvM space indicates their stage in evolution. Most clouds are confined to the region between the adiabat and the inversion layer base except for small precipitating (lower left region) and dissipating clouds (upper left region). The color shades of the clouds indicate whether a cloud is mostly core (red), mostly margin (blue), or equally divided to core and margin (white).

As seen for the single cloud, the core mass fractions tend to be larger than core volume fractions, for all core types. This is due to the fact that LWC values in the cloud core regions are higher than in margin regions, so that a cloud might be core dominated in

terms of mass while being margin dominated in terms of volume. Focusing on the differences between core types, the color patterns in the CvM space imply that B_{core} definition yields the lowest core fractions (for both mass and volume), followed by RH_{core} with higher values and W_{core} with the highest values. The absence of the B_{core} is especially noticeable for small clouds in their initial growth stages after formation (COG ~ 550 m and LWP < 1 g m^{-2}). Those same clouds show the highest core fractions for the other two core definitions. This large difference can be explained by the existence of the transition layer (as discussed in Sect. 3) near the lifting condensation level (LCL) in warm convective cloud fields which is the approximated height of a convective cloud base (Craven et al., 2002; Meerkötter and Bugliaro, 2009). Within this layer parcels rising from the sub-cloudy layer are generally colder than parcels subsiding from the cloudy layer. Thus, this transition layer clearly marks the lower edge of the buoyancy core as most convective clouds are initially negatively buoyant.

Generally, the growing cloud branch (i.e. the CvM region closest to the adiabat) shows the highest core fractions. The RH_{core} and W_{core} fractions decrease with cloud growth (increase in mass and COG height) while the B_{core} initially increases, shows the highest fraction values around the middle region of the growing branch and then decreases for the largest clouds. The transition from the growing branch to the dissipation branch is manifested by a transition from core dominated to margin dominated clouds (i.e. transition from red to blue shades). Mixed within the margin dominated dissipating cloud branch, a scatter of W_{core} dominated small clouds can be seen as well. These represent cloud fragments which shed off large clouds during their growing stages with positive vertical velocity. They are sometimes RH_{core} dominated as well but are strictly negatively buoyant. The few precipitating cloud fragments seen for this simulation (cloud scatter located below the adiabat) tend to be margin dominated, especially for the RH_{core}.

5.2. Subset properties of cores

From Fig. 4 it is clear that W_{core} tends to be the largest and B_{core} tends to be the smallest. To what degree however, are the cores subsets of one another as was seen for the single cloud simulation? It is also interesting to check whether the different physical

cores are centered near the cloud's geometrical core. In Fig. 5 the pixel fraction (f_{pixel}) of each core type within another core type is shown for all clouds in the CvM space. A f_{pixel} of 1 (bright colors) indicates that the pixels of the specific core in question (labeled in each panel title) are a subset of the other core (also labeled in the panel title) and a f_{pixel} of 0 (dark colors) indicates no intersection between the two cores in the cloud. It is seen that B_{core} tends to be a subset of both other cores, with f_{pixel} around 0.75-1 for most of the growing branch area and large mass dissipating clouds which still have some positive buoyancy. The pixel fractions are higher for B_{core} inside W_{core} compared with B_{core} inside RH_{core}, but both show decrease with increase in growing branch cloud mass, meaning the chance for finding a proper subset B_{core} decreases in large clouds.

The CvM space of RH_{core} inside W_{core} shows an even stronger relation between these two core types. For almost all growing branch clouds, the RH_{core} is a subset of W_{core} (i.e. $RH_{core} \subseteq W_{core}$). The decrease gradually with loss of cloud mass in the dissipation branch. The other three permutations of f_{pixel} (W_{core} inside B_{core}, W_{core} inside RH_{core}, and RH_{core} inside B_{core}) give an indication of cores sizes and of which cloud types show no overlap between different cores. As stated above, growing (dissipation) clouds show higher (lower) overlap between the different core types. The W_{core} is almost twice as large as the B_{core} and 30% - 40% larger than the RH_{core} along most of the growing branch. In conclusion, we see a strong tendency for the subset property of cores ($B_{core} \subseteq RH_{core} \subseteq W_{core}$) during the growth stages of clouds. This property ceases for dissipating and precipitating clouds, especially for the smaller clouds which show less overlap between core types.

In Fig. 6 the normalized distances (D_{norm}) between the total cloud centroid and each specific physical core centroid locations are evaluated. Along the growing branch the cloud centroid and physical cores' centroids tend to be of close proximity, while during cloud dissipation the cores' centroids tend to increase in distance from the cloud's center. This type of evolution is most prominent for the W_{core}, which shows a clear gradient of transition from small (dark colors) to large (bright colors) distances. The B_{core} shows a more complex transition, from intermediate distance values (~0.5) at cloud formation, to near zeros values along the mature part of the growing branch, back to large values in the dissipation branch. Along the growing branch RH_{core} shows

distances comparable to the W_{core} (except for large distances at cloud formation). However, compared to the other two core types, RH_{core} shows the smallest distances to the geometrical core during cloud dissipation. This is manifested by a relative absence of bright colors for dissipating clouds in Fig. 6.

The prevalence of cloud edge B_{core} pixels during dissipation can be explained by adiabatic heating due to weak downdrafts (see Sect. 4.2, Part II) which are expected at the cloud periphery. The fact that there is little overlap between B_{core} and both W_{core} and RH_{core} pixels in dissipating clouds (see Fig. 5) serves to verify this assumption. The relative absence of isolated RH_{core} pixels at the cloud edges can be explained by the fact the pixels closest to the cloud's edge are most susceptible to mixing with non-cloudy air and evaporation, yielding subsaturation conditions. The innermost pixels are "protected" from such mixing and thus we can expect most RH_{core} pixels to be located near the geometrical core.

The W_{core} case is less intuitive. During cloud dissipation complex patterns of updrafts and downdrafts within the cloud can create scenarios where the W_{core} centroid is located anywhere in the cloud. However, the results show that most small dissipating clouds tend to have their W_{core} pixels concentrated at the cloud edges. Comparing Fig. 6 with Figs. 4 and 5, we can see that these pixels comprise only a tiny fraction of the already small clouds and do not overlap with RH_{core} and B_{core} pixels and thus are not related to significant convection processes. Further analysis shows that the maximum updrafts in these clouds rarely exceed 0.5 m/s (i.e. 90% of clouds with normalized distance > 0.9 have a maximum updraft of less than 0.5 m/s), and can thus be considered with near neutral vertical velocity.

5.3. Consistency of the cloud partition to core types

The results for cloud fields are summarized in Fig. 7 that presents the evolution of core fractions of continuous cloud entities (CCEs, see Sect. 2.5 for details) from formation to dissipation. Only CCEs that undergo a complete life cycle are averaged here. These CCEs fulfill the following four conditions: i) form near the LCL, ii) live for at least 10 minutes, ii) reach maximum cloud mean LWP values above 10 g m^{-2}, and iv) terminate with mass value below 10 g m^{-2}. As a test of generality, we performed this analysis for

Hawaiian and CASS warm cumulus cloud field simulations in addition to the BOMEX one. For each simulation, hundreds of CCEs are collected (see panel titles) and their core volume fractions are averaged according to their normalized lifetimes (τ).

Consistent results are seen for all three simulations. Clouds initiate with a W_{core} fraction of ~ 1, RH_{core} fraction of ~ 0.8, and B_{core} fraction of ~ 0 - 0.1. The former two core types' volume fraction decreases monotonically with lifetime, while the latter core type's volume fraction increases up to 0.15 - 0.35 at $\tau \sim 0.25$, and then monotonically decreases for increasing τ. The continental (CASS) simulation consistently shows lower buoyancy volume fractions than the oceanic simulations. This can be attributed to lower RH in the CASS cloudy layer (60% - 80%) compared with the oceanic simulations (85% - 95%. The lower RH increases entrainment and reduces buoyancy. The fact that clouds end their life cycle with non-zero volume fractions may indicate that some of the CCE terminate not because of full dissipation but rather because of significant splitting or merging events.

Normalized distances (D_{norm}) between core centroid and total cloud centroid (Fig. 7, middle column) tend to monotonically increase for RH_{core} and W_{core} with CCE lifetime for all simulations. The gradient of increase is larger at the later stages of CCE lifetime. Initially the W_{core} is closer to the geometrical core but at later stages of CCE lifetime (typically $\tau > 0.5$) this switches and RH_{core} remains the closest. As seen above, for the first (second) half of CCE lifetime, the distance between B_{core} centroid and cloud centroid decreases (increases), starting at normalized distances above 0.4 for all simulations. The physical cores stay closer to the geometrical core ($D_{norm} < 0.5$) for the majority of their lifetimes for the three cases. However, the assumption that a cloud's core (by any definition) is also indicative of the cloud's centroid only applies to a fraction of that lifetime. Taking the value $D_{norm} = 0.25$ as a threshold for physical cores centered near the cloud centroid, Bomex, Hawaii, and CASS simulation CCEs' W_{core} cross this threshold at $\tau = 0.8$, 0.6, and 0.65, respectively. Thus, the core-shell geometrical model is mostly true for the first two-thirds of a typical cloud's lifetime.

The analysis of core subset properties (Fig. 7, right column) shows that the assumption $B_{core} \subseteq RH_{core} \subseteq W_{core}$ is true for the initial formation stages of a cloud. Although the corresponding pixel fractions decrease slightly during the lifetime of the CCE, they remain above 0.9 (e.g. B_{core} is 90% contained within RH_{core}). A sharp decrease in

pixel fractions is seen for $\tau > 0.8$ ($\tau > 0.5$ for the CASS simulation), as the overlaps between the different cores is reduced during dissipation stages of the cloud. For all simulations, the highest pixel fraction values are seen for the B_{core} inside W_{core} pair, followed by RH_{core} inside W_{core} pair, and B_{core} inside RH_{core} pair showing lower values. In addition, it can be seen that the variance of average pixel fraction (per τ) increases with increase in τ. This is due to the fact the all CCEs initiate with almost identical characteristics but may terminate in very different ways. In part II of this work we show that this variance is highly influenced from precipitation which contributes to more significant interactions between clouds (Heiblum et al., 2016b).

6. Summary

In this paper we study the partition of warm convective clouds to core and margin according to three different definitions: i) positive vertical velocity (W_{core}), ii) relative humidity supersaturation (RH_{core}), and iii) positive buoyancy (B_{core}), with emphasis on the differences between those definitions. Using theoretical considerations of both an adiabatic cloud column and a simple two parcel mixing model (see appendix A and B), we support our simulated results as we show that the B_{core} is expected to be the smallest of the three. This finding is in line with previous works that showed that negative buoyancy is prevalent in cumulus clouds for a wide range of thermodynamic conditions (de Roode, 2008; Paluch, 1979; Taylor and Baker, 1991). This is due to the fact that entrainment into the core (i.e. mixing with non-cloudy environment or mixing with the margin regions of the cloud) may result in sub-saturation, followed by evaporation that always has a negative net effect on buoyancy. The same process has an opposing effect on the relative humidity of the mixed parcel and acts to reach saturation. Entrainment (or mixing) also acts to decrease vertical velocity, but at slower manner compared to the time scales of changes in the buoyancy and relative humidity. In addition, the supersaturation equation (Eq. (3)) predicts that it is unlikely to maintain supersaturation in a cloudy volume with negative vertical velocity. Hence, W_{core} can be expected to be the largest of the three cores.

Using numerical simulations of both a single cloud and cloud fields of warm cumulus clouds, we show that during most stages of clouds' lifetime, W_{core} is indeed the largest

of the three and B_{core} the smallest. In addition to the differences in their sizes, the three cores tend to be subsets of one another (and located around the cloud geometrical center), in the following order: $B_{core} \subseteq RH_{core} \subseteq W_{core}$. This property is most valid for a cloud at its initial stages and breaks down gradually during a cloud's lifetime. The warm convective cloud fields simulated here typically have a transition layer near the lifting condensation level (LCL). Thus, the lower parts of the clouds are negatively buoyant or even lack a B_{core} at formation. After cloud formation internal growth processes (i.e. condensation and latent heat release) increase the B_{core} until dissipation processes become dominant and the B_{core} decreases quickly due to entrainment. In contrast, clouds are initially dominated by the W_{core} and RH_{core} (fractions close to 1). The fractions of these cores then decrease monotonically with cloud lifetime.

During dissipation stages, the clouds are mostly margin dominated, such that most of the small mass dissipation cloud fragments are entirely coreless. However, several small mass dissipating cloud fragments which shed off large cloud entities (with large COG height) may be core dominated, especially using the RH_{core} definition. The same is observed for small precipitating cloud fragments which reside below the convective cloud base. We note that the results here are similar for both volume and mass core fractions out the cloud's totals, with the core mass fractions being larger due to a skewed distribution of cloud LWC which favors the core regions. Moreover, we show that these results are consistent for various levels of aerosol concentrations (will be seen in Part II) and different thermodynamic profiles used to initialize the models.

With respect to cloud morphology, it is shown that during cloud growth, which comprises the majority of a warm cloud lifetime, the physical cores are centered near the cloud's geometrical core, as is intuitively expected from a cloud's core. This matches the convective cloud core-shell model. An exception to this is the initial growth stages, where the B_{core} centroid can be located far from the cloud's centroid. During dissipation (i.e. approximately the last third of a cloud's lifetime), the core-shell model no longer applies to the clouds, as the cores decouple from the geometrical core and often comprise just a few isolated pixels at the cloud's edges. The W_{core} and B_{core} pixels tend to be more peripheral than RH_{core} during dissipation (see Sect. 5.2). Downdraft induced adiabatic heating at the clouds' edge (see more in Part II) promote positive buoyancy while decreasing the chance for supersaturation. During dissipation

689 the overlap between different core types also decreases rapidly, implying that minor
690 local effects enable core existence rather than cloud convection. Thus, only during
691 mature growth stages can all three cores types can be considered interchangeable. In
692 Part II of this work we use the insights gained here to understand aerosol effects on
693 warm convective clouds, as are reflected by a cloud's partition to its core and margin.

694

695 **Acknowledgements**
696 The research leading to these results was supported by the Ministry of Science &
697 Technology, Israel (grant no. 3-14444).

698

699

700 **Appendix A: Buoyancy changes due to mixing of cloudy and non-cloudy parcels**

701 Here we present a simple model for entrainment mixing between a cloudy parcel (either
702 part of B_{core} or B_{margin}) and a dry environmental parcel. Entrainment mixes the
703 momentum, heat, and humidity of the two parcels. We consider the mixing of a unit
704 mass of cloud parcel which is defined by two criteria:

705 $$S_1 \geq 1$$
$$B_1 > 0 \; or \; B_1 < 0$$

706 with a unit mass of dry environment parcel, defined by:

707 $$S_2 < 1$$

708 and explore the properties of the resulting mixed parcel.

709 Assume that T_1, T_2, T_3 are the initial temperatures of the cloudy, environmental, and
710 resulting mixed parcel, respectively. q_{v1}, q_{v2}, q_{v3}, $\theta_1, \theta_2, \theta_3$, and $q_{l_1}, q_{l_2}, q_{l_3}$ are their
711 respective vapor mixing ratios, potential temperatures, and liquid water contents
712 (LWC).

713 The change in buoyancy due to mixing will be:

714 $$dB_{mix} = g * \left(\frac{\theta_3 - \theta_1}{\theta_2} + 0.61(q_{v3} - q_{v1}) - (q_{l_3} - q_{l_1})\right) \quad \text{(A1)},$$

715 with

716 $T_3 = \mu_1 \cdot T_1 + \mu_2 \cdot \mathrm{T}_2$ (A2),

717 $q_{v3} = \mu_1 \cdot q_{v1} + \mu_2 \cdot q_{\mathrm{v2}}$ (A3),

718 $q_{l_3} = \mu_1 \cdot q_{l_1} + \mu_2 \cdot q_{l_2}$ (A4),

719 where μ_1 and μ_2 are the corresponding mixing fractions. We assume that the mixed
720 parcel is at the same height as the cloudy and environmental parcels, and that the mean
721 environmental temperature at that height stays the same after mixing. The potential
722 temperature (θ) is calculated using its definition.

723 After the mixing process, the resultant mixed parcel may be subsaturated ($S_3 < 1$), and
724 cloud droplets start to evaporate. The evaporation process increases the humidity of the
725 parcel. ((Korolev et al., 2016), Eq. (A8)) calculated the amount of the required liquid
726 water for evaporation, in order to reach S=1 again:

727 $$\delta q = \frac{C_p R_v T_2^2}{L^2} ln\left(\frac{1+\frac{e_s(T_3)R_a L^2}{PC_p R_v^2 T_3^2}}{1+S_3\frac{e_s(T_3)R_a L^2}{PC_p R_v^2 T_3^2}}\right)$$ (A5),

728 Where C_p is a specific heat at constant pressure,$e_s(T_3)$ is the saturated vapor pressure
729 for the mixed temperature, P is pressure, L is latent heat, R_v, R_a are individual gas
730 constants for water vapor and dry air, respectively. If the mixed parcel contains
731 sufficient LWC to evaporate δq amount of water, the mixed parcel will reach
732 saturation. We note that Eq. (A5) holds for cases where $|T_1 - T_2| < 10^o C$, which is
733 well within the range seen in our simulations of warm clouds.

734 Assuming the average environmental temperature stays the same after evaporation, the
735 buoyancy after evaporation is calculated using the following formulas:

736 $$dB_{evap} = g \cdot \left(\frac{d\theta'_{evap}}{\theta_2} + 0.61 dq_{v_{evap}} - dq_{l_{evap}}\right)$$ (A6),

737 $$d\theta'_{evap} = dT_{evap}$$ (A7),

738 From the first law of thermodynamics:

739 $$C_p \cdot dT_{evap} = -L \cdot dq_{v_{evap}}$$ (A8).

740 The water vapor is the amount of liquid water lost by evaporation:

741 $$dq_{v_{evap}} = -dq_{l_{evap}} = \delta q \quad \text{(A9)},$$

742 From the above we get:

743 $$dB_{evap} = g \cdot \delta q \left(1.61 - \frac{L}{C_p \theta_2}\right) \quad \text{(A10)}.$$

744 For a wide temperature range between $200 < \theta_2 < 300[K]$, dB_{evap} is always
745 negative. This result is not trivial because evaporation both decreases the T and
746 increases the q_v which have opposite effects. The total change in buoyancy is taken as
747 the sum of dB_{evap} and dB_{mix}.

748 Figure A1 presents a phase space of possible changes in cloudy pixel buoyancy due to
749 mixing with outside air, for various thermodynamic conditions, and a mixing fraction
750 of 0.5. The initial cloudy parcel is chosen to be saturated (S=1) and includes a LWC of
751 1 g kg^{-1}. The pressure is assumed to be 850 mb, and the temperature 15ºC. However,
752 we note that the conclusions here apply to all atmospherically relevant values of
753 pressure, temperature, supersaturation (values of RH>100%), and LWC in warm
754 clouds. The X-axis in Fig. A1 spans a range of non-cloudy environment relative
755 humidity values (60% < RH < 100%), and the Y-axis spans a temperature difference
756 range between the cloud and the environment parcels ($-3° < dT < 3°$). The initial (B_i)
757 and final (B_f, after entrainment) buoyancy values, and the differences between them
758 can be either positive or negative. The regions of $B_i>0$ ($B_i<0$) in fact illustrate the effects
759 of entrainment on B_{core} (B_{margin}) parcels.

760

761

762 **Appendix B**: **Buoyancy changes due to mixing of core and margin parcels**

763 Following the notations of appendix A, we now consider the mixing of two cloudy
764 parcels, one part of B_{core} and one part ofB_{margin}. For simplicity, we choose the case
765 where both parcels are saturated and have the same LWC of 0.5 g kg^{-1}:

766 $$\begin{matrix} S_{core} = S_{margin} = S_{cloud} = 1 \\ q_{l_{core}} = q_{l_{margin}} = q_{l_{cloud}} = 0.5 \end{matrix} \quad \text{(B1)}.$$

The buoyancy of each cloudy parcel is determined in reference to the environmental temperature and humidity, $T_{env}, q_{v_{env}}$, so that:

$$B_{cloud} = g * \left(\frac{\theta_{cloud}-\theta_{env}}{\theta_{env}} + 0.61\left(q_{v_{cloud}} - q_{v_{env}}\right) - q_{l_{cloud}}\right) \quad \text{(B2)}.$$

As mentioned in the main text, we take a temperature range of $T_{env} - 3°c < T_{cloud} < T_{env} + 3°c$. Each cloudy parcel's temperature also dictates its saturation vapor pressure $e_s(T_{cloud})$ and therefore also its humidity content, $q_{v_{cloud}}$. Plugging these into Eq. (B2), one can associate each temperature/humidity pair with the B_{core} or B_{margin}:

$$\begin{matrix} T_{core} = T_{cloud}(B_{cloud} > 0),\ q_{v_{core}} = q_{v_{cloud}}(B_{cloud} > 0) \\ T_{margin} = T_{cloud}(B_{cloud} < 0), q_{v_{margin}} = q_{v_{cloud}}(B_{cloud} < 0) \end{matrix} \quad \text{(B3)}.$$

The core and margin parcels can then be mixed (see appendix A) yielding a mixed parcel temperature and humidity content, and thus a new relative humidity. The buoyancy of the mixed parcel is obtained by inserting these parameters in Eq. (B2).

In Fig. B1 the resultant buoyancy values and RH values after the mixing of B_{core} parcels with B_{margin} parcels are shown. As defined in Appendix A, temperature differences between the parcels and the environment are confined to ±3°C. The reference environmental temperature, pressure, and RH are taken to be 15°C, 850 mb, and 90%, respectively. We note the main differences between this section and Appendix A are the absence of evaporation and the fact that the core and margin thermodynamic variables are the ones that vary while the reference environmental ones are kept constant.

It can be seen that all negatively buoyant parcels are colder than the environment and nearly all positively buoyant parcels are warmer than the environment, except for a small fraction that are slightly colder but positively buoyant due to the increased humidity. The transition from $B_f>0$ to $B_f<0$ near the 1 to 1 line indicates that B_f is approximately linearly dependent on the temperature differences with respect to the environment. In other words, if $|T_{core} - T_{env}|>\left|T_{margin} - T_{env}\right|$, the mixed parcel is expected to be part of the B_{core} (i.e. $B_f>0$). The exponential increase in saturation vapor pressure with temperature is demonstrated by the results of the mixed parcel final RH, which all show supersaturation values. Additional sensitivity tests were performed for

this analysis, showing only weak dependencies on environmental parameter values, while maintaining the main conclusions.

References

Ackerman, B.: Buoyancy and precipitation in tropical cumuli, J. Meteor., 13(3), 302–310, doi:10.1175/1520-0469(1956)013<0302:BAPITC>2.0.CO;2, 1956.

Altaratz, O., Koren, I., Reisin, T., Kostinski, A., Feingold, G., Levin, Z. and Yin, Y.: Aerosols' influence on the interplay between condensation, evaporation and rain in warm cumulus cloud, Atmos. Chem. Phys., 8(1), 15–24, doi:10.5194/acp-8-15-2008, 2008.

Betts, A. K.: Non-precipitating cumulus convection and its parameterization, Q.J Royal Met. Soc., 99(419), 178–196, doi:10.1002/qj.49709941915, 1973.

Burnet, F. and Brenguier, J.-L.: The onset of precipitation in warm cumulus clouds: An observational case-study, Q.J Royal Met. Soc., doi:10.1002/qj.552, 2010.

Craven, J. P., Jewell, R. E. and Brooks, H. E.: Comparison between Observed Convective Cloud-Base Heights and Lifting Condensation Level for Two Different Lifted Parcels, Wea. Forecasting, 17(4), 885–890, doi:10.1175/1520-0434(2002)017<0885:CBOCCB>2.0.CO;2, 2002.

Dagan, G., Koren, I. and Altaratz, O.: Competition between core and periphery-based processes in warm convective clouds – from invigoration to suppression, Atmos. Chem. Phys., 15(5), 2749–2760, doi:10.5194/acp-15-2749-2015, 2015.

Dawe, J. T. and Austin, P. H.: Statistical analysis of an LES shallow cumulus cloud ensemble using a' ' cloud tracking algorithm, Atmos. Chem. Phys., 12(2), 1101–1119, doi:10.5194/acp-12-1101-2012, 2012.

de Roode, S. R.: Thermodynamics of cumulus clouds, Física de la Tierra; Vol 19 (2007), 2008.

de Roode, S. R. and Bretherton, C. S.: Mass-Flux Budgets of Shallow Cumulus Clouds, J. Atmos. Sci., 60(1), 137–151, doi:10.1175/1520-0469(2003)060<0137:MFBOSC>2.0.CO;2, 2003.

de Roode, S. R., Siebesma, A. P., Jonker, H. J. J. and de Voogd, Y.: Parameterization of the vertical velocity equation for shallow cumulus clouds, Mon. Wea. Rev., 140(8), 2424–2436, doi:10.1175/MWR-D-11-00277.1, 2012.

de Rooy, W. C. and Siebesma, A. P.: A simple parameterization for detrainment in shallow cumulus, Mon. Wea. Rev., 136(2), 560–576, doi:10.1175/2007MWR2201.1, 2008.

Derbyshire, S. H., Maidens, A. V., Milton, S. F., Stratton, R. A. and Willett, M. R.: Adaptive detrainment in a convective parametrization, Q.J Royal Met. Soc., 137(660), 1856–1871, doi:10.1002/qj.875, 2011.

Emanuel, K. A.: A Scheme for Representing Cumulus Convection in Large-Scale Models, J. Atmos. Sci., 48(21), 2313–2329, doi:10.1175/1520-0469(1991)048<2313:ASFRCC>2.0.CO;2, 1991.

Feingold, G., Levin, Z. and Tzivion (Tzitzvashvili), S.: The evolution of raindrop spectra. part III: downdraft generation in an axisymmetrical rainshaft model, J. Atmos. Sci., 48(2), 315–330, doi:10.1175/1520-0469(1991)048<0315:TEORSP>2.0.CO;2, 1991.

Feingold, G., Tzivion (Tzitzvashvili), S. and Leviv, Z.: Evolution of raindrop spectra. part I: solution to the stochastic collection/breakup equation using the method of moments, J. Atmos. Sci., 45(22), 3387–3399, doi:10.1175/1520-0469(1988)045<3387:EORSPI>2.0.CO;2, 1988.

Garstang, M. and Betts, A. K.: A review of the tropical boundary layer and cumulus convection: structure, parameterization, and modeling, Bull. Amer. Meteor. Soc., 55(10), 1195–1205, doi:10.1175/1520-0477(1974)055<1195:AROTTB>2.0.CO;2, 1974.

Grabowski, W. W. and Jarecka, D.: Modeling condensation in shallow nonprecipitating convection, J. Atmos. Sci., 72(12), 4661–4679, doi:10.1175/JAS-D-15-0091.1, 2015.

Grant, A. L. M. and Lock, A. P.: The turbulent kinetic energy budget for shallow cumulus convection, Q.J Royal Met. Soc., 130(597), 401–422, doi:10.1256/qj.03.50, 2004.

Gregory, D. and Rowntree, P. R.: A Mass Flux Convection Scheme with Representation of Cloud Ensemble Characteristics and Stability-Dependent Closure, Mon. Wea. Rev., 118(7), 1483–1506, doi:10.1175/1520-0493(1990)118<1483:AMFCSW>2.0.CO;2, 1990.

Heiblum, R. H., Altaratz, O., Koren, I., Feingold, G., Kostinski, A. B., Khain, A. P., Ovchinnikov, M., Fredj, E., Dagan, G., Pinto, L., Yaish, R. and Chen, Q.: Characterization of cumulus cloud fields using trajectories in the center of gravity

versus water mass phase space: 1. Cloud tracking and phase space description, J. Geophys. Res. Atmos., 121(11), 6336–6355, doi:10.1002/2015JD024186, 2016a.

Heiblum, R. H., Altaratz, O., Koren, I., Feingold, G., Kostinski, A. B., Khain, A. P., Ovchinnikov, M., Fredj, E., Dagan, G., Pinto, L., Yaish, R. and Chen, Q.: Characterization of cumulus cloud fields using trajectories in the center of gravity versus water mass phase space: 2. Aerosol effects on warm convective clouds, J. Geophys. Res. Atmos., 121(11), 6356–6373, doi:10.1002/2015JD024193, 2016b.

Hernandez-Deckers, D. and Sherwood, S. C.: A numerical investigation of cumulus thermals, J. Atmos. Sci., 73(10), 4117–4136, doi:10.1175/JAS-D-15-0385.1, 2016.

Heus, T., J. Pols, C. F., J. Jonker, H. J., A. Van den Akker, H. E. and H. Lenschow, D.: Observational validation of the compensating mass flux through the shell around cumulus clouds, Q.J Royal Met. Soc., 135(638), 101–112, doi:10.1002/qj.358, 2009a.

Heus, T. and Jonker, H. J. J.: Subsiding Shells around Shallow Cumulus Clouds, J. Atmos. Sci., 65(3), 1003–1018, doi:10.1175/2007JAS2322.1, 2008.

Heus, T., Jonker, H. J. J., Van den Akker, H. E. A., Griffith, E. J., Koutek, M. and Post, F. H.: A statistical approach to the life cycle analysis of cumulus clouds selected in a virtual reality environment, J. Geophys. Res., 114(D6), doi:10.1029/2008JD010917, 2009b.

Heus, T. and Seifert, A.: Automated tracking of shallow cumulus clouds in large domain, long duration large eddy simulations, Geosci. Model Dev., 6(4), 1261–1273, doi:10.5194/gmd-6-1261-2013, 2013.

Holland, J. Z. and Rasmusson, E. M.: Measurements of the Atmospheric Mass, Energy, and Momentum Budgets Over a 500-Kilometer Square of Tropical Ocean, Mon. Wea. Rev., 101(1), 44–55, doi:10.1175/1520-0493(1973)101<0044:MOTAME>2.3.CO;2, 1973.

IPCC: Climate Change 2013: The Physical Science Basis. Working Group I Contribution to the Fifth Assessment Report of the IPCC, Cambridge Univ. Press, New York., 2013.

Jaenicke, R.: 9.3.1 Physical properties, in Physical and chemical properties of the air, edited by G. Fischer, pp. 405–420, Springer-Verlag, Berlin/Heidelberg., 1988.

Jiang, H. and Feingold, G.: Effect of aerosol on warm convective clouds: Aerosol-cloud-surface flux feedbacks in a new coupled large eddy model, J. Geophys. Res., 111(D1), doi:10.1029/2005JD006138, 2006.

Jonker, H. J. J., Heus, T. and Sullivan, P. P.: A refined view of vertical mass transport by cumulus convection, Geophys. Res. Lett., 35(7), doi:10.1029/2007GL032606, 2008.

Kain, J. S. and Fritsch, J. M.: A One-Dimensional Entraining/Detraining Plume Model and Its Application in Convective Parameterization, J. Atmos. Sci., 47(23), 2784–2802, doi:10.1175/1520-0469(1990)047<2784:AODEPM>2.0.CO;2, 1990.

Khain, A., Pokrovsky, A., Pinsky, M., Seifert, A. and Phillips, V.: Simulation of Effects of Atmospheric Aerosols on Deep Turbulent Convective Clouds Using a Spectral Microphysics Mixed-Phase Cumulus Cloud Model. Part I: Model Description and Possible Applications, J. Atmos. Sci., 61(24), 2963–2982, doi:10.1175/JAS-3350.1, 2004.

Khairoutdinov, M. F., Krueger, S. K., Moeng, C.-H., Bogenschutz, P. A. and Randall, D. A.: Large-eddy simulation of maritime deep tropical convection, J. Adv. Model. Earth Syst., 2, 15, doi:10.3894/JAMES.2009.1.15, 2009.

Khairoutdinov, M. F. and Randall, D. A.: Cloud resolving modeling of the ARM summer 1997 IOP: model formulation, results, uncertainties, and sensitivities, J. Atmos. Sci., 60(4), 607–625, doi:10.1175/1520-0469(2003)060<0607:CRMOTA>2.0.CO;2, 2003.

Korolev, A., Khain, A., Pinsky, M. and French, J.: Theoretical study of mixing in liquid clouds – Part 1: Classical concepts, Atmos. Chem. Phys., 16(14), 9235–9254, doi:10.5194/acp-16-9235-2016, 2016.

Kumar, V. V., Jakob, C., Protat, A., Williams, C. R. and May, P. T.: Mass-Flux Characteristics of Tropical Cumulus Clouds from Wind Profiler Observations at Darwin, Australia, J. Atmos. Sci., 72(5), 1837–1855, doi:10.1175/JAS-D-14-0259.1, 2015.

Lebo, Z. J. and Seinfeld, J. H.: Theoretical basis for convective invigoration due to increased aerosol concentration, Atmos. Chem. Phys., 11(11), 5407–5429, doi:10.5194/acp-11-5407-2011, 2011.

Lehmann, K., Siebert, H. and Shaw, R. A.: Homogeneous and inhomogeneous mixing in cumulus clouds: Dependence on local turbulence structure, Journal of the Atmospheric Sciences, 66(12), 3641–3659, 2009.

Malkus, J. S.: On the structure of the trade wind moist layer, Woods Hole Oceanographic Institution, Woods Hole, MA., 1957.

Meerkötter, R. and Bugliaro, L.: Diurnal evolution of cloud base heights in convective cloud fields from MSG/SEVIRI data, Atmos. Chem. Phys., 9(5), 1767–1778, doi:10.5194/acp-9-1767-2009, 2009.

Morrison, H.: On the robustness of aerosol effects on an idealized supercell storm simulated with a cloud system-resolving model, Atmos. Chem. Phys., 12(16), 7689–7705, doi:10.5194/acp-12-7689-2012, 2012.

Morrison, H.: Impacts of updraft size and dimensionality on the perturbation pressure and vertical velocity in cumulus convection. part I: simple, generalized analytic solutions, J. Atmos. Sci., 73(4), 1441–1454, doi:10.1175/JAS-D-15-0040.1, 2016.

Morrison, H.: An analytic description of the structure and evolution of growing deep cumulus updrafts, J. Atmos. Sci., 74(3), 809–834, doi:10.1175/JAS-D-16-0234.1, 2017.

Neggers, R. A. J., Stevens, B. and Neelin, J. D.: Variance scaling in shallow-cumulus-topped mixed layers, Q.J Royal Met. Soc., 133(628), 1629–1641, doi:10.1002/qj.105, 2007.

Paluch, I. R.: The entrainment mechanism in colorado cumuli, J. Atmos. Sci., 36(12), 2467–2478, doi:10.1175/1520-0469(1979)036<2467:TEMICC>2.0.CO;2, 1979.

Peters, J. M.: The Impact of Effective Buoyancy and Dynamic Pressure Forcing on Vertical Velocities within Two-Dimensional Updrafts, J. Atmos. Sci., 73(11), 4531–4551, doi:10.1175/JAS-D-16-0016.1, 2016.

Pinsky, M., Mazin, I. P., Korolev, A. and Khain, A.: Supersaturation and diffusional droplet growth in liquid clouds, J. Atmos. Sci., 70(9), 2778–2793, doi:10.1175/JAS-D-12-077.1, 2013.

Reisin, T., Levin, Z. and Tzivion, S.: Rain Production in Convective Clouds As Simulated in an Axisymmetric Model with Detailed Microphysics. Part I: Description of the Model, J. Atmos. Sci., 53(3), 497–519, doi:10.1175/1520-0469(1996)053<0497:RPICCA>2.0.CO;2, 1996.

Rennó, N. O. and Ingersoll, A. P.: Natural convection as a heat engine: A theory for CAPE, J. Atmos. Sci., 53(4), 572–585, doi:10.1175/1520-0469(1996)053<0572:NCAAHE>2.0.CO;2, 1996.

Rodts, S. M. A., Duynkerke, P. G. and Jonker, H. J. J.: Size Distributions and Dynamical Properties of Shallow Cumulus Clouds from Aircraft Observations and Satellite Data, J. Atmos. Sci., 60(16), 1895–1912, doi:10.1175/1520-0469(2003)060<1895:SDADPO>2.0.CO;2, 2003.

Rogers, R. R. and Yau, M. K.: A Short Course in Cloud Physics, International Series in Natural Philosophy, 1989.

Romps, D. M. and Charn, A. B.: Sticky Thermals: Evidence for a Dominant Balance between Buoyancy and Drag in Cloud Updrafts, J. Atmos. Sci., 72(8), 2890–2901, doi:10.1175/JAS-D-15-0042.1, 2015.

Seigel, R. B.: Shallow Cumulus Mixing and Subcloud-Layer Responses to Variations in Aerosol Loading, J. Atmos. Sci., 71(7), 2581–2603, doi:10.1175/JAS-D-13-0352.1, 2014.

971 Siebesma, A. P., Bretherton, C. S., Brown, A., Chlond, A., Cuxart, J., Duynkerke, P.
972 G., Jiang, H., Khairoutdinov, M., Lewellen, D., Moeng, C.-H., Sanchez, E., Stevens,
973 B. and Stevens, D. E.: A large eddy simulation intercomparison study of shallow
974 cumulus convection, J. Atmos. Sci., 60(10), 1201–1219, doi:10.1175/1520-
975 0469(2003)60<1201:ALESIS>2.0.CO;2, 2003.

976 Siebesma, A. P. and Cuijpers, J. W. M.: Evaluation of parametric assumptions for
977 shallow cumulus convection, J. Atmos. Sci., 52(6), 650–666, doi:10.1175/1520-
978 0469(1995)052<0650:EOPAFS>2.0.CO;2, 1995.

979 Sinkevich, A. A. and Lawson, R. P.: A survey of temperature measurements in
980 convective clouds, J. Appl. Meteor., 44(7), 1133–1145, doi:10.1175/JAM2247.1,
981 2005.

982 Taylor, G. R. and Baker, M. B.: Entrainment and detrainment in cumulus clouds, J.
983 Atmos. Sci., 48(1), 112–121, doi:10.1175/1520-
984 0469(1991)048<0112:EADICC>2.0.CO;2, 1991.

985 Trenberth, K. E., Fasullo, J. T. and Kiehl, J.: Earth's global energy budget, Bull.
986 Amer. Meteor. Soc., 90(3), 311–323, doi:10.1175/2008BAMS2634.1, 2009.

987 Tzivion (Tzitzvashvili), S., Feingold, G. and Levin, Z.: The evolution of raindrop
988 spectra. part II: collisional collection/breakup and evaporation in a rainshaft, J.
989 Atmos. Sci., 46(21), 3312–3328, doi:10.1175/1520-
990 0469(1989)046<3312:TEORSP>2.0.CO;2, 1989.

991 Tzivion, S., Reisin, T. and Levin, Z.: Numerical simulation of hygroscopic seeding in
992 a convective cloud, J. Appl. Meteor., 33(2), 252–267, doi:10.1175/1520-
993 0450(1994)033<0252:NSOHSI>2.0.CO;2, 1994.

994 Wang, Y., Geerts, B. and French, J.: Dynamics of the cumulus cloud margin: an
995 observational study, J. Atmos. Sci., 66(12), 3660–3677, doi:10.1175/2009JAS3129.1,
996 2009.

997 Wei, D., Blyth, A. M. and Raymond, D. J.: Buoyancy of convective clouds in TOGA
998 COARE, Journal of the atmospheric sciences, 55(22), 3381–3391, 1998.

999 Williams, E. and Stanfill, S.: The physical origin of the land–ocean contrast in
1000 lightning activity, Comptes Rendus Physique, 3(10), 1277–1292, doi:10.1016/S1631-
1001 0705(02)01407-X, 2002.

1002 Xue, H. and Feingold, G.: Large-Eddy Simulations of Trade Wind Cumuli:
1003 Investigation of Aerosol Indirect Effects, J. Atmos. Sci., 63(6), 1605–1622,
1004 doi:10.1175/JAS3706.1, 2006.

1005 Yano, J.-I., Chaboureau, J.-P. and Guichard, F.: A generalization of CAPE into
1006 potential-energy convertibility, Q.J Royal Met. Soc., 131(607), 861–875,
1007 doi:10.1256/qj.03.188, 2005.

Figures

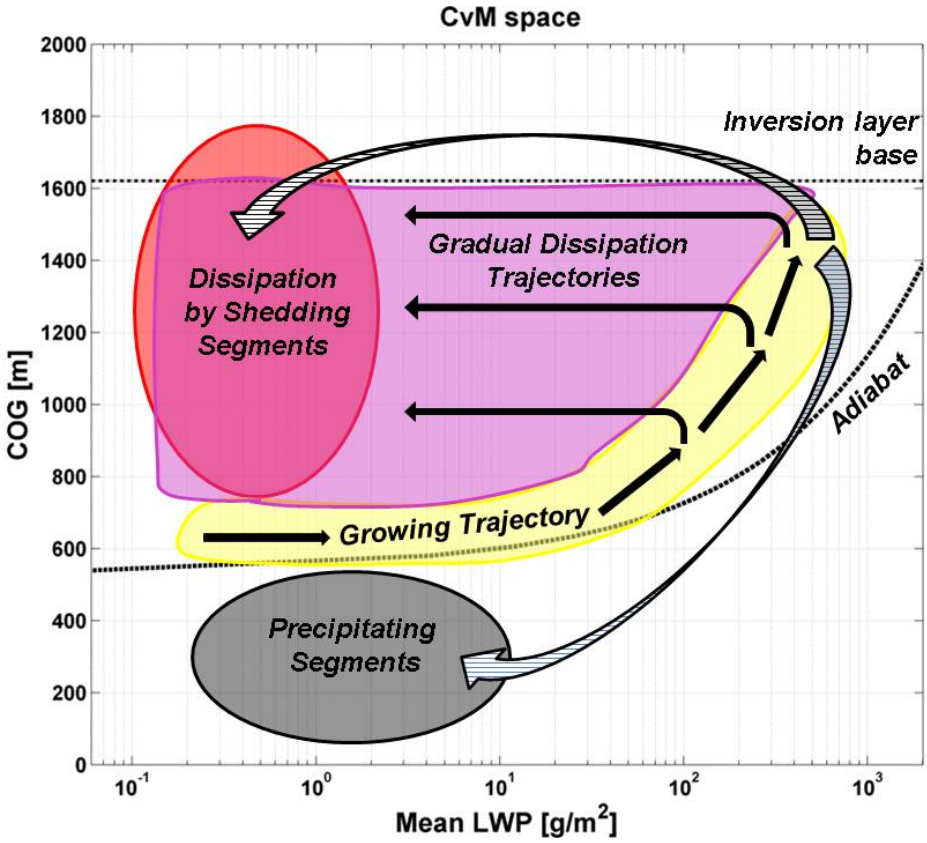

Figure 1. A schematic representation of a cloud field Center-of-gravity height (Y-Axis) vs. Mass (X-Axis) phase space (CvM in short). The majority of clouds are confined to the region between the adiabatic approximation (curved dashed line) and the inversion layer base height (horizontal dashed line). The yellow, magenta, red, and grey shaded regions represent cloud growth, gradual dissipation, cloud fragments which shed off large clouds, and cloud fragments which shed off precipitating clouds, respectively. The black arrows represent continuous trajectories of cloud growth and dissipation. The hatched arrows represent two possible discontinuous trajectories of cloud dissipation where clouds shed segments.

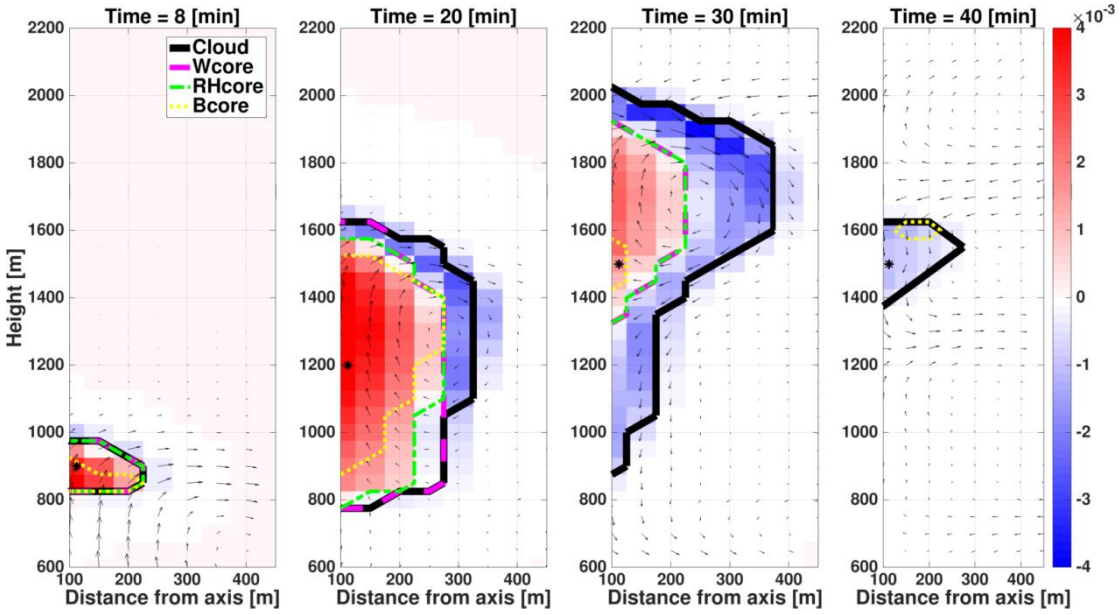

Figure 2. Four vertical cross-sections (at t=8, 20, 30, 40 minutes) during the single cloud simulation. Y-axis represents height [m] and X-axis represents the distance from the axis [m]. The black, magenta, green and yellow lines represent the cloud, W_{core}, RH_{core} and B_{core}, respectively. The black arrows represent the wind, the background represents the condensation (red) and evaporation rate (blue) [g kg^{-1} s^{-1}], and the black asterisks indicate the vertical location of the cloud centroid. Note that in some cases the lines indicating core boundaries overlap (mainly seen for RH and W cores).

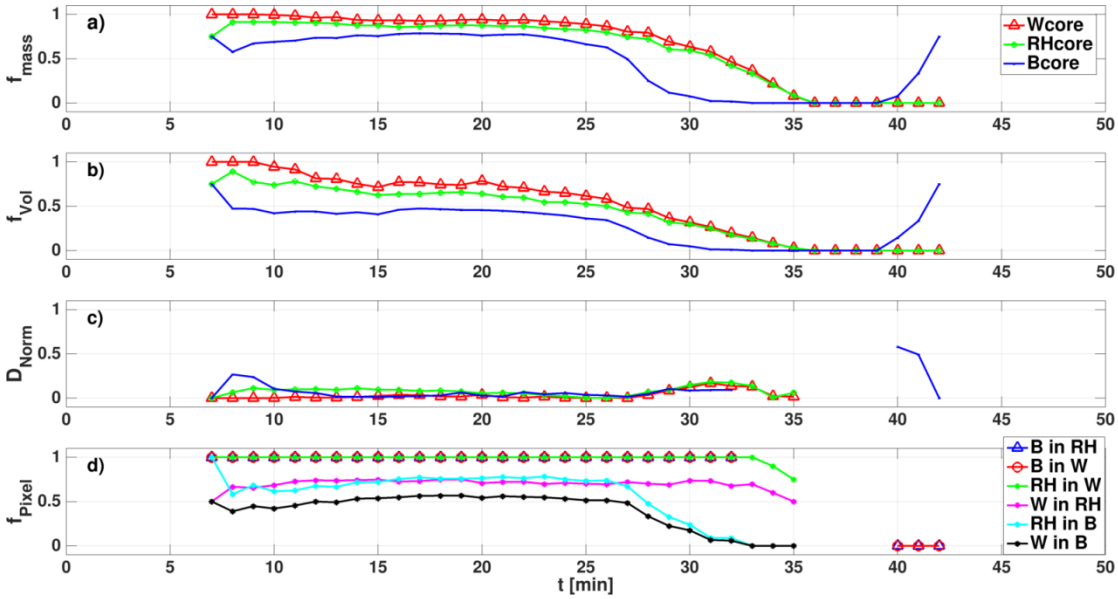

Figure 3. Temporal evolution of selected core properties, including: (a) The fraction of the cores' mass from the total cloud mass (f_{mass}), (b) the fraction of the cores' volume from the total cloud volume (f_{vol}), (c) the normalized distance between cloud centroid and core centroid (D_{norm}), and (d) the fraction of cores' pixels contained within another core (f_{pixel}), including all six permutations. See panel legends for descriptions of line colors.

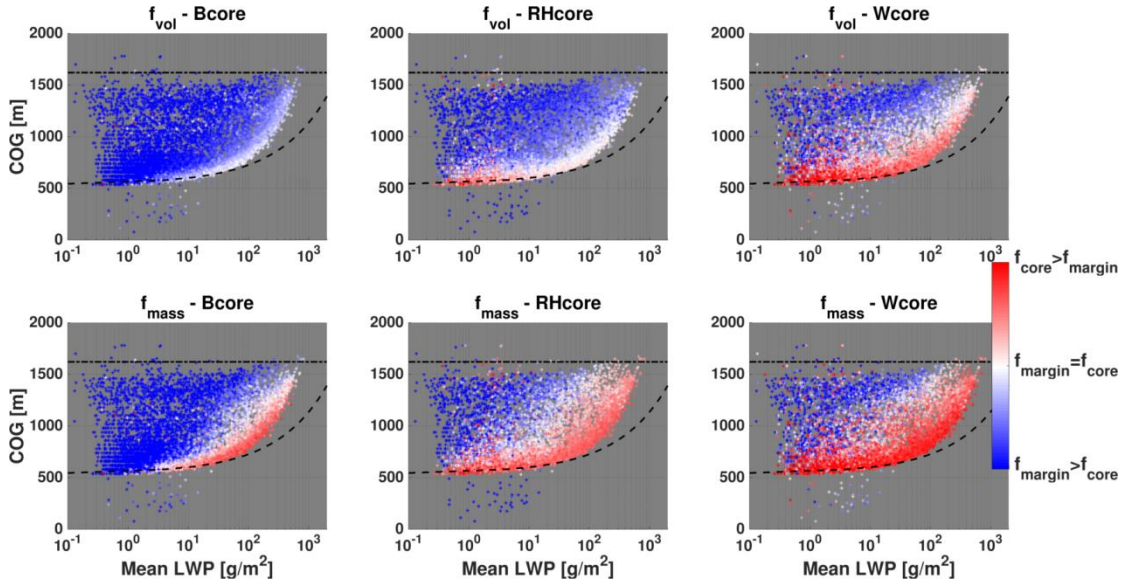

Figure 4. CvM phase space diagrams of B_{core} (left column), RH_{core} (middle column), and W_{core} (right column) fractions for all clouds between 3 h and 8 h in the BOMEX simulation. Both volume fractions (f_{vol}, upper panels) and mass fractions (f_{mass} lower panels) are shown. The red (blue) colors indicate a core fraction above (below) 0.5. For a general description of CvM space characteristics the reader is referred to Sect. 2.4.

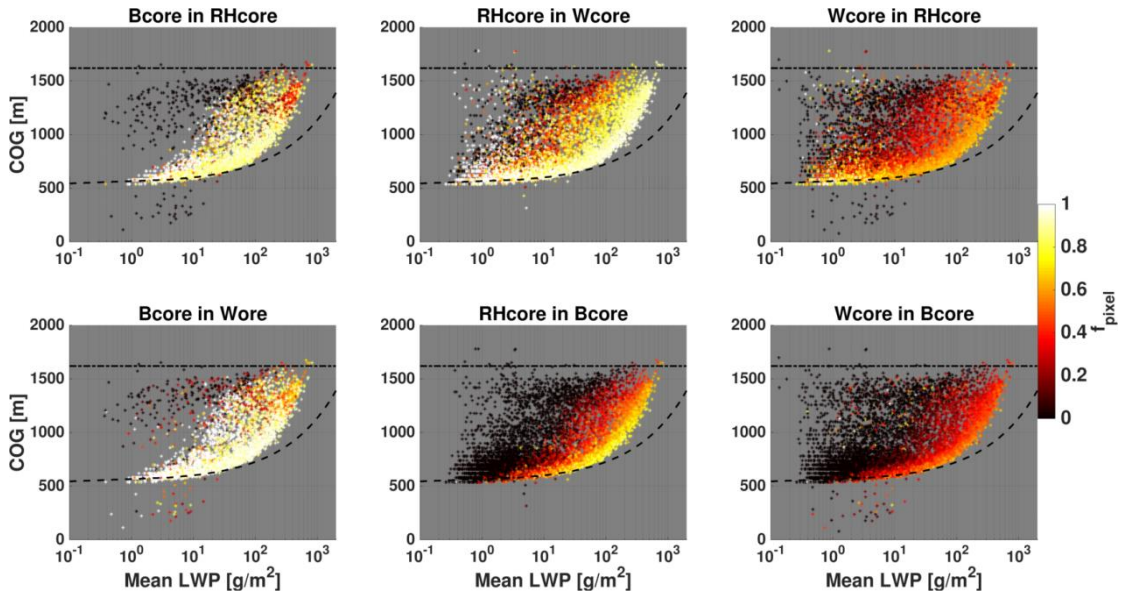

Figure 5. CvM phase space diagrams of pixel fractions (f_{pixel}) of each of the three cores within another core, including six different permutations (as indicated in the panel titles). Bright colors indicate high pixel fractions (large overlap between two core types) while dark colors indicate low pixel fraction (little overlap between two core types). The differences in the scatter density and location for different panels are due to the fact that only clouds which contain a core fraction above zero (for the core in question) are considered. For example, for the Buoy in RH panel (upper left), only cloud that contain some pixels with positive buoyancy are considered.

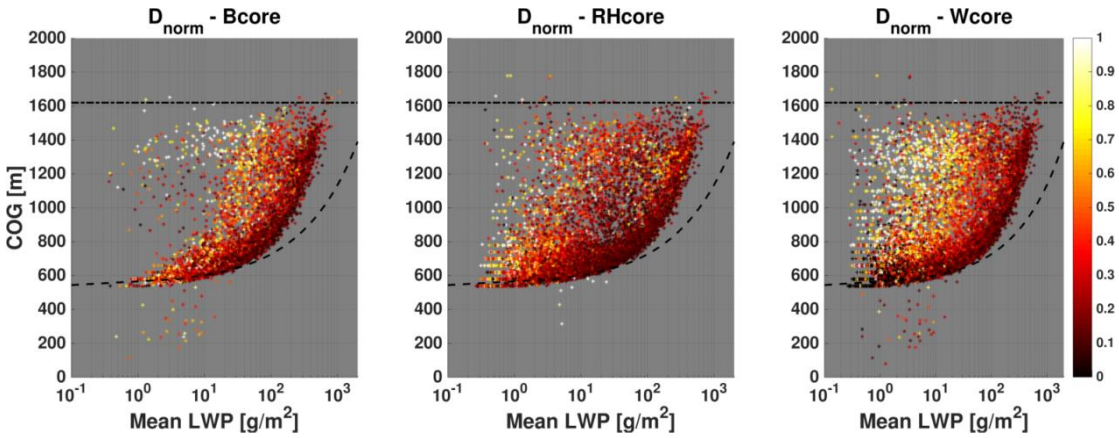

Figure 6. CvM phase space diagrams of distances between core centroid location and cloud centroid location, for the three different physical core types. The distances are normalized by the cloud volume radius (approximately the largest distance possible). Bright (dark) colors indicates large (small) distances. As seen in Fig. 5, only clouds which contain a core fraction above zero (for the core in question) are considered.

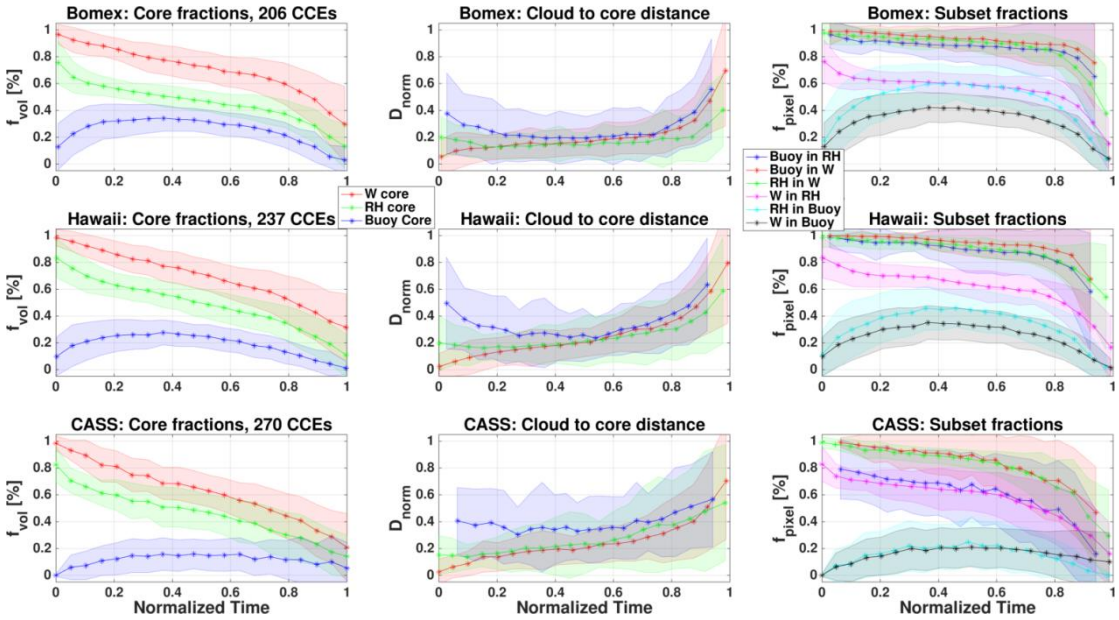

Figure 7. Normalized time series of CCE averaged core fractions for the BOMEX (upper row), Hawaii (middle row), and CASS (bottom row) simulations. Both core volume fractions (f_{vol}, left column), normalized distances between cloud and core centroid locations (D_{norm}, middle column), and pixel fractions of one core within another (f_{pixel}, right column) are considered. Line colors indicated different core types (see legends), while corresponding shaded color regions indicate the standard deviation. Normalized time enables to average together CCEs with different lifetimes, from formation to dissipation. The number of CCEs averaged together for each simulation is included in the left column panel titles.

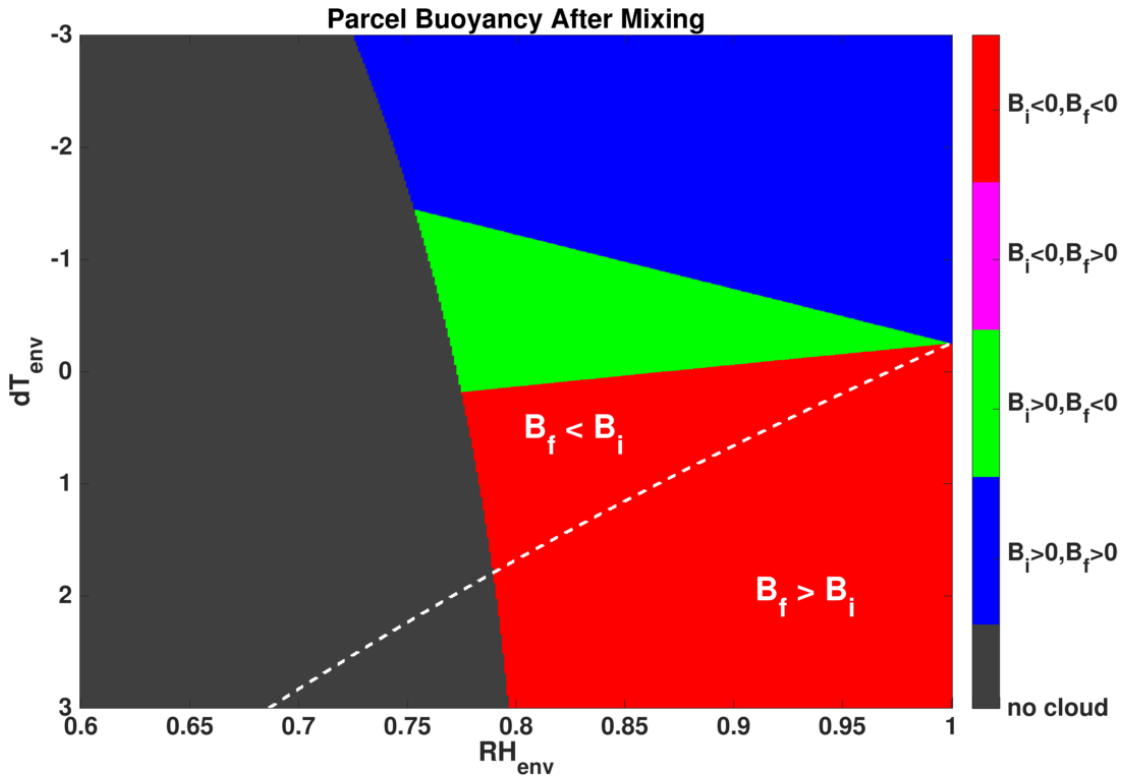

Figure A1. Phase space presenting the effects of entrainment on cloud buoyancy, where the initial cloudy parcel buoyancy (Bi) and final mixed parcel buoyancy (Bf) are considered. A mixing fraction of 0.5 is chosen. The initial cloudy parcel is saturated (S=1), has a temperature of 15°C, pressure of 850 mb, and LWC of 1 g kg^{-1}. The X-axis spans a range of environment relative humidity values (RH_{env}), and the Y-axis a temperature difference ($dT_{env}=T_{env}-T_{cld}$) range between the cloud and the environment parcels. Red color represents B_i <0 & B_f <0 (i.e. parcel stays negatively buoyant after the mixing), magenta represents B_i <0 & B_f >0 (i.e. transition from negative to positive buoyancy), green represents B_i >0 & B_f <0 (i.e. transition from positive to negative buoyancy), and blue represents B_i >0 & B_f >0 (i.e. parcel stays positively buoyant). The grey color represents mixed parcels that were depleted from water (LWC value lower than 0.01 g kg^{-1}) after evaporation, and are considered non-cloudy. The white line separates between areas where $B_f > B_i$ and $B_f < B_i$.

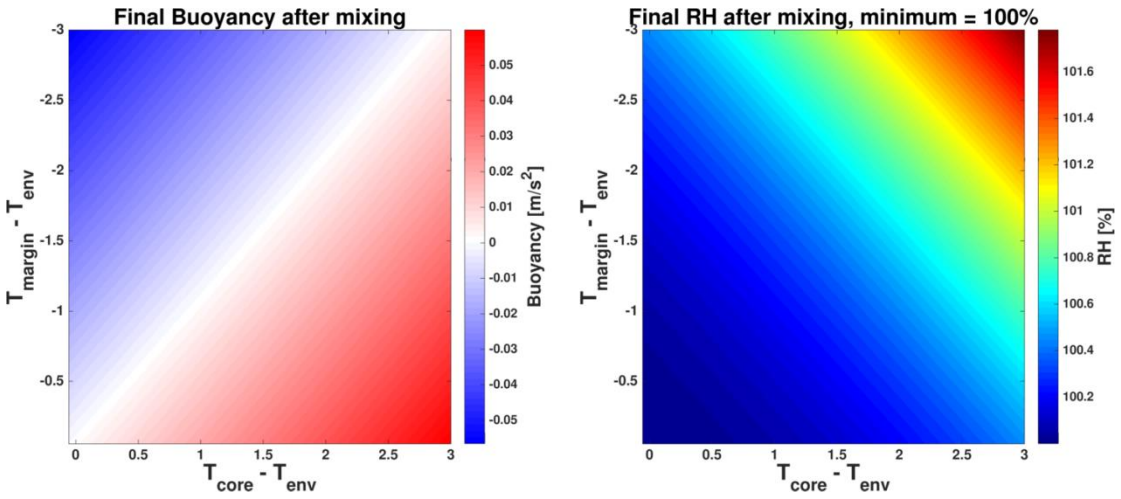

Figure B1. Phase space presenting the resultant buoyancy (left panel) and relative humidity (RH, right panel) when mixing B_{core} and B_{margin} parcels with equal RH but different temperatures. A mixing fraction of 0.5 is chosen. Both parcels are initially saturated (RH=100%), and have a LWC of 0.5 g kg^{-1}. The environment has a temperature of 15^{o}C and pressure of 850 mb. The X(Y)-axis spans the range of temperature differences between the B_{core} (B_{margin}) parcel and the environment.